PAPER • OPEN ACCESS

PCO and hardware delay calibration for LEO satellite antenna downlinking navigation signals

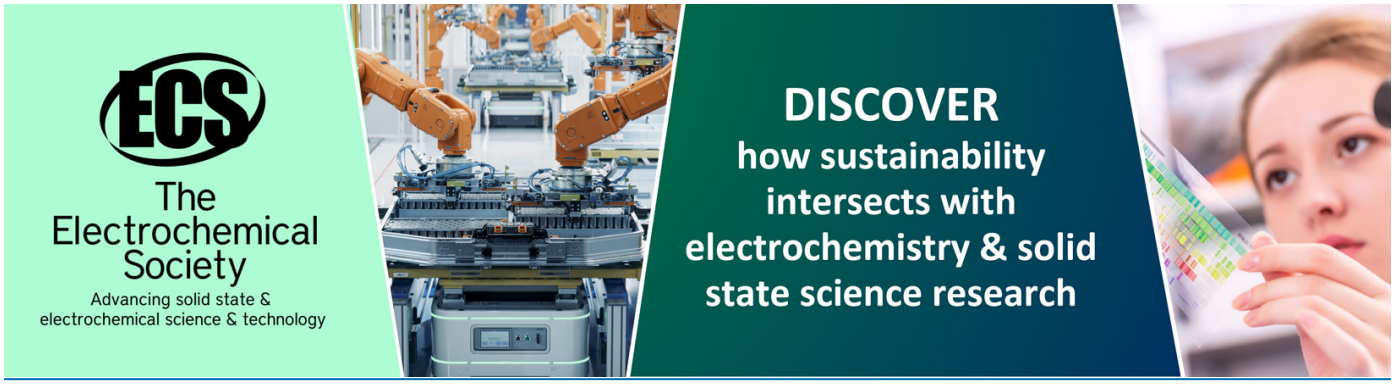

OPEN ACCESS
IOP Publishing
Measurement Science and Technology
Meas. Sci. Technol. **35** (2024) 086314 (16pp)
https://doi.org/10.1088/1361-6501/ad48a2

PCO and hardware delay calibration for LEO satellite antenna downlinking navigation signals

Jiawei Liu[1,3], **Kan Wang**[1,2,3,*], **Ahmed El-Mowafy**[4] and **Xuhai Yang**[1,2,3]

[1] National Time Service Center, Chinese Academy of Sciences, Xi'an, People's Republic of China
[2] University of Chinese Academy of Sciences, Beijing, People's Republic of China
[3] Key Laboratory of Time Reference and Applications, Chinese Academy of Sciences, Xi'an, People's Republic of China
[4] School of Earth and Planetary Sciences, Curtin University, Perth, Australia

E-mail: wangkan@ntsc.ac.cn

Received 27 February 2024, revised 17 April 2024
Accepted for publication 8 May 2024
Published 21 May 2024

Abstract

Augmentation of the Global Navigation Satellite System by low earth orbit (LEO) satellites is a promising approach benefiting from the advantages of LEO satellites. This, however, requires errors and biases in the satellite downlink navigation signals to be calibrated, modeled, or eliminated. This contribution introduces an approach for in-orbit calibration of the phase center offsets (PCOs) and code hardware delays of the LEO downlink navigation signal transmitter/antenna. Using the satellite geometries of Sentinel-3B and Sentinel-6A as examples, the study analyzed the formal precision and bias influences for potential downlink antenna PCOs and hardware delays of LEO satellites under different ground network distributions, and processing periods. It was found that increasing the number of tracking stations and processing periods can improve the formal precision of PCOs and hardware delay. Less than 3.5 mm and 3 cm, respectively, can be achieved with 10 stations and 6 processing days. The bias projections of the real-time LEO satellite orbital and clock errors can reach below 3 mm in such a case. For near-polar LEO satellites, stations in polar areas are essential for strengthening the observation model.

Keywords: low earth orbit (LEO), global navigation satellite system (GNSS), phase center offset (PCO), position, navigation and timing (PNT), hardware delay

1. Introduction

Over the past decade, many countries have embarked on launching low earth orbit (LEO) satellite constellations for diverse applications, including communications, mapping, remote sensing, and navigation augmentation [1–3]. The quantity of both currently operational and planned LEO satellites has surged, reaching tens of thousands. The increasing number of LEO satellites has brought opportunities for their use in augmentation of traditional Global Navigation Satellite System (GNSS)-based positioning, navigation, and timing [4–6]. Benefiting from the lower altitudes and higher speeds of LEO satellites, the augmentation of the GNSS by LEO satellites has numerous advantages, including providing hundreds to thousands of times stronger signal strength than the GNSS satellites [7], the more rapid convergence time of precise point positioning (PPP) and the PPP-Real-Time Kinematic positioning due to the rapid geometry change [8–10]. The faster speed of the LEO satellites also helps to whiten multipath effects, which changes the behaviors of these typically mismodelled

* Author to whom any correspondence should be addressed.

biases attributing them mostly to noise [11]. In addition to the above advantages, since LEO satellites move in middle layers between the GNSS satellites and the ground users, the use of LEO satellites for integrity monitoring of the GNSS signals and products, and near-real-time broadcast of navigation integrity monitoring alarm information, was also discussed [12].

To achieve high-accuracy positioning and timing on the ground using LEO navigation signals, the errors and biases in the downlink navigation signals between LEO satellites and ground users must be precisely calibrated, modeled, or eliminated. These errors include LEO satellite orbital and clock errors, ground receiver clock errors, tropospheric delays, ionospheric delays, phase ambiguities, phase center offsets (PCOs) and phase center variations (PCVs), and various hardware delays. For instance, the errors of GNSS satellite PCO for PPP can reach the centimeter level [13], and the hardware delay of the differential code biases (DCBs) can reach more than ten nanoseconds [14].

When using GNSS signals for positioning, the GNSS satellite orbital and clock errors are often determined based on GNSS data collected by a ground network [15–19]. The obtained satellite clock errors often contain the Ionosphere-Free (IF) code hardware delays of the downlink navigation signal transmitter/antenna. Ground users only apply appropriate DCBs according to the type of code observations used [20–22]. In contrast to GNSS satellite orbital and clock products that are computed based on signals tracked by a ground tracking network, LEO satellites have a significantly smaller footprint on the Earth's surface due to their lower orbital altitudes, which can both lead to difficulties in continuous tracking of the LEO satellite navigation signals. As a result, high-accuracy LEO satellite orbital and clock products are often determined using the GNSS signals tracked onboard instead of those tracked by ground stations. Depending on the LEO satellite precise orbit determination (POD) approach, the GNSS signals and products used, the computational power, and the latency required, precise LEO satellite orbital and clock errors can be determined at a few centimeters to dm-level [23, 24].

However, the estimated orbital errors that are typically at the LEO satellite Center of Mass (CoM) and the clock errors, which contain IF code hardware delays of the onboard GNSS receiver/antenna, are not products that can be directly used by ground users. These users need the LEO satellite orbits computed at the downlink Antenna Phase Center (APC), and the clock errors that contain the IF code hard biases of the downlink navigation signal transmitter/antenna. Consequently, for LEO satellite clock products, as an example, a two-step adjustment process is needed to support the ground-based positioning and timing services. First, the IF code hardware delay of the onboard GNSS receiver and antenna contained in the estimated LEO satellite clock errors must be accounted for. Second, the IF code hardware delay of the LEO satellite's downlink navigation signal transmitter and antenna needs to be added. Both types of hardware delays can be calibrated on the ground before launching LEO satellites. However, these hardware delays could vary in-orbit compared to those calibrated on the ground, in-orbit calibration is thus needed for high-accuracy positioning services. The IF code hardware delays of the LEO satellite's onboard GNSS receiver and antenna can be estimated using the GNSS signals, whereas those of the downlink signal transmitter/antenna require strategies for in-orbit calibration. Similar to the hardware delays, the PCOs of the downlink navigation antenna need in-orbit calibration, as the in-orbit PCOs could vary by a few centimeters from those calibrated on the ground [25].

Similar to the GNSS satellites, the in-orbit calibration of the LEO satellite PCOs and hardware delays of the downlink signal transmitter/antenna can only be performed using the downlinked navigation signals collected by ground stations. However, considering the small footprints of LEO satellites and the foreseeable shortage of ground stations capable of receiving LEO navigation signals in the near future, great challenges exist for the in-orbit calibration of these terms. This particularly invites an appropriate approach, and if applicable, additional information in the calibration process as described below:

(1) In [26, 27], a strong correlation between hardware delays and temperature was shown for GNSS antennas. In [24], the systematic effects contained in GRACE Follow-on satellite estimable clock parameters are also suspected to be related to temperature-related hardware biases. As such, as long as the temperature data are available for the in-orbit calibration process, the first-order derivative term of the hardware delays related to temperature can be estimated in addition to the offset delays.
(2) GNSS observations tracked by the same ground stations can be fully used to determine ground-based parameters such as station coordinates, receiver clock errors and zenith tropospheric delays.
(3) Considering the high correlation between the PCOs and hardware delays of the LEO satellite downlink signal transmitters/antennas, it is suggested to estimate and use them together, so that a combined high precision can be achieved.
(4) In this study, PCVs of the LEO satellite downlink antenna are not estimated. Similar to GNSS, it is expected that the PCVs of the LEO satellite downlink antenna to be small compared to the PCOs, i.e. in sub-millimeters to millimeters in most cases. However, the PCV of the LEO satellite downlink antenna is certainly an interesting topic to be investigated when real LEO satellite navigation signals become available in the future.

After the introduction, this paper starts with presenting the approach for determining the LEO satellite's downlink navigation signal PCOs and the IF code hardware delay. This includes the strategy for evaluating their formal precision and influences of diverse mismodelled biases projected on the PCOs and IF code hardware delay of the downlink signal antenna. Afterward, taking two types of LEO satellites with

different inclination angles as examples, the Observed-Minus-Computed (O-C) terms of the downlink dual-frequency navigation signals are simulated. The formal precision and the range-projected bias of the PCOs and hardware delays are analyzed for different ground network distributions and processing intervals. The conclusions are outlined at the end.

2. Processing strategy

This section is split into two parts. The strategy of in-orbit calibration for the PCOs and IF code hardware delays of the LEO satellite's downlink signals is first introduced. Subsequently, the evaluation methods of the estimable parameters are shortly discussed.

2.1. In-orbit calibration of the PCO and code hardware delays of the downlink antenna

The in-orbit calibration of the PCO and IF code hardware delays of the LEO satellite's downlink navigation signal antenna are performed in three steps as described in this section.

2.1.1. Determination of the initial LEO satellite APCs and clock errors for downlink purposes. First, the high-precision LEO satellite orbits and the clock errors (containing the onboard GNSS receiver/antenna IF code hardware delays) need to be post-processed within the POD procedure [28–34]. Applying the on-ground calibration of the PCOs and hardware delays of the LEO satellite downlink antennas, the initial APC orbits and clock errors for downlink purposes can be calculated. The detailed calculation process to obtain the initial APC orbits and clock errors is illustrated by the flow chart in figure 1.

Equation (1) formulates the initial LEO satellite APC orbits in the Earth-Centered Earth-Fixed (ECEF) system as follows:

$$\hat{x}^{Ls0} = \hat{x}^{Ls}_{\mathrm{APC}} - R_{\mathrm{NEUG2ECEF}}\Delta\hat{x}^{Ls}_{\mathrm{PCO,GNSS}} - R_{\mathrm{B2ECEF}}\Delta x^{Ls}_{\mathrm{CoM2ARPG}} + R_{\mathrm{B2ECEF}}\Delta x^{Ls}_{\mathrm{CoM2ARPL}} + R_{\mathrm{NEU2ECEF}}\Delta x^{Ls0}_{\mathrm{PCO}} \quad (1)$$

where $\hat{x}^{Ls}_{\mathrm{APC}}$ denotes the LEO satellite orbits at the APC of the onboard GNSS antenna obtained from the POD process. $\Delta\hat{x}^{Ls}_{\mathrm{PCO,GNSS}}$ denotes the LEO satellite North, East, and Up (NEU) components of the GNSS antenna PCO based on an in-orbit calibration. $\Delta x^{Ls0}_{\mathrm{PCO}}$ represents the LEO satellite PCO (NEU components) of the downlink navigation antenna based on on-ground calibration. $\Delta x^{Ls}_{\mathrm{CoM2ARPG}}$ denotes the vector from the LEO satellite CoM to the GNSS antenna Antenna Reference Point (ARP), given in the LEO satellite body-fixed system. $\Delta x^{Ls}_{\mathrm{CoM2ARPL}}$ is the vector from the LEO satellite CoM to the downlink antenna ARP, given in the LEO satellite body-fixed system. $R_{\mathrm{NEUG2ECEF}}$ denotes the rotation matrix from the satellite onboard GNSS antenna system to the ECEF coordinate system, and R_{NEU2ECEF} denotes that from the downlink antenna system to the ECEF. The two rotation matrices can be expressed as:

$$R_{\mathrm{NEUG2ECEF}} = R_{\mathrm{B2ECEF}}R_{\mathrm{NEUG2B}} \quad (2)$$

$$R_{\mathrm{NEU2ECEF}} = R_{\mathrm{B2ECEF}}R_{\mathrm{NEU2B}} \quad (3)$$

where R_{NEUG2B} and R_{NEU2B} are the rotation matrices from the satellite onboard GNSS antenna system and the downlink antenna system to the LEO satellite body-fixed coordinate system, respectively. Both of the rotation matrices depend on the direction of the corresponding antennas on the LEO satellite denotes the rotation matrix from the LEO satellite body-fixed system to the ECEF system, which can be further expressed as:

$$R_{\mathrm{B2ECEF}} = R_{\mathrm{ECI2ECEF}}R_{\mathrm{B2ECI}} \quad (4)$$

for which R_{ECI2ECEF} is the rotation matrix from the Earth-Centered Inertial (ECI) system (here J2000.0) to the ECEF system, and represents the rotation matrix from the satellite body-fixed system to the ECI system, which can be calculated by the attitude quaternions, i.e. q_0, q_1, q_2 and q_3 are given as follows [35–37]:

$$R_{\mathrm{B2ECI}} = \begin{pmatrix} 1-2\times(q_2^2+q_3^2) & 2\times(q_1q_2-q_0q_3) & 2\times(q_1q_3+q_0q_2) \\ 2\times(q_1q_2+q_0q_3) & 1-2\times(q_1^2+q_3^2) & 2\times(q_2q_3-q_0q_1) \\ 2\times(q_1q_3-q_0q_2) & 2\times(q_2q_3+q_0q_1) & 1-2\times(q_1^2+q_2^2) \end{pmatrix}. \quad (5)$$

In case the attitude information of the LEO satellite is unknown, the nominal attitude can be used for further processing. The nominal attitude is often defined based on the radial and velocity directions of the LEO satellites, e.g. the x-axis of the body-fixed system along the velocity direction, and the z-axis against the radial direction. This definition gives the rotation matrix from the body-fixed system to the RTA system in the radial (R), along-track (T), and cross-track directions (A), i.e. as follows:

$$R_{\mathrm{B2RTA}} = \begin{pmatrix} 0 & 0 & -1 \\ \delta & 0 & 0 \\ 0 & -\delta & 0 \end{pmatrix}. \quad (6)$$

Depending on the specific definition of the body-fixed system by different LEO satellites at different periods, the factor δ can be taken either as 1 or -1. For example, if the definition

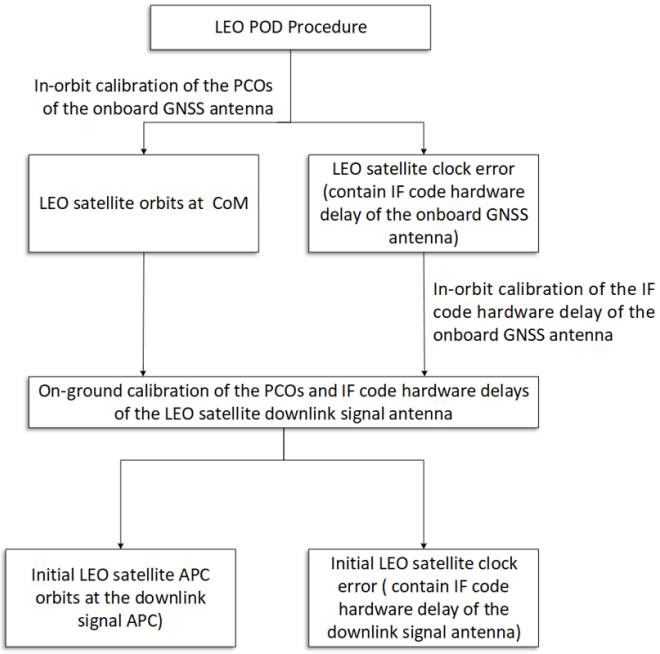

Figure 1. The flowchart of calculating the initial LEO APC orbits and clock errors.

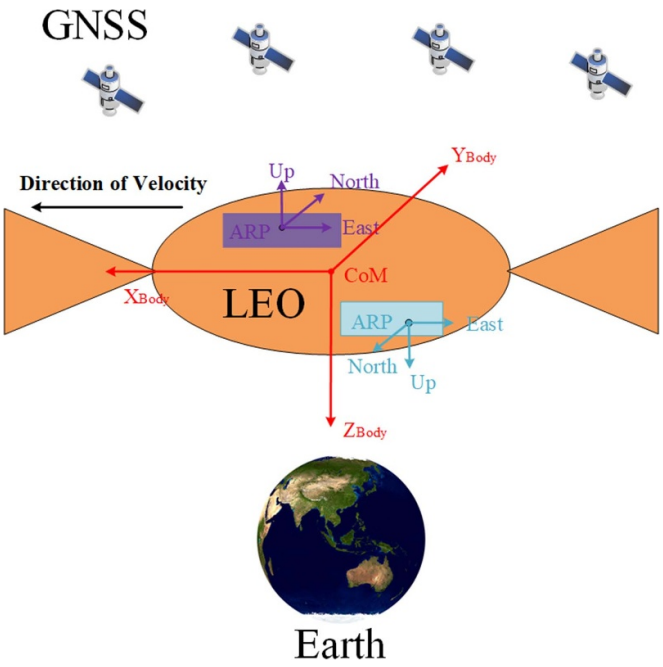

Figure 2. LEO satellite body-fixed system and different antenna systems. The LEO satellite Sentinal-6A is used as an example here.

of a body-fixed system is $[X, Y, Z] = [T, -A, -R]$, then δ is 1, which means the x-axis points along the velocity direction (i.e. direction of the satellite motion).

With R_{B2RTA} defined, to obtain the R_{B2ECEF} in equation (4), one needs to determine the rotation matrix between the RTA system and the ECEF system (R_{RTA2ECEF}) for usage of the nominal attitude using the LEO satellite position and velocity. The rotation matrix from the body-fixed system to the ECEF system can thus be determined by:

$$R_{\mathrm{B2ECEF}} = R_{\mathrm{RTA2ECEF}} R_{\mathrm{B2RTA}}. \tag{7}$$

To solve equations (2) and (3), the rotation matrices from the antenna NEU systems to the body-fixed system need to be known. Taking the antenna systems in figure 2 as an example, the transformation matrices for the on-board GNSS antenna and the downlink antenna, i.e. R_{NEUG2B} and R_{NEU2B} can be expressed as:

$$R_{\mathrm{NEUG2B}} = \begin{pmatrix} 0 & -1 & 0 \\ 1 & 0 & 0 \\ 0 & 0 & -1 \end{pmatrix} \tag{8}$$

$$R_{\mathrm{NEU2B}} = \begin{pmatrix} 0 & -1 & 0 \\ -1 & 0 & 0 \\ 0 & 0 & 1 \end{pmatrix} \tag{9}$$

All elements on the right side of equations (2) and (3) can be obtained with or without the attitude quaternions, and the initial LEO satellite APC orbits ($\hat{x}^{Ls0}$) for downlink purposes can be calculated accordingly.

The initial value of the LEO satellite clock errors ($\widetilde{dt}^{\,\wedge Ls0}$) for downlink purposes can be expressed as:

$$\widetilde{dt}^{\,\wedge Ls0}(t_i) = \widehat{dt}^{\,Ls}(t_i) + \frac{d_{\mathrm{IF}}^{Ls0} + T^{Ls}(t_i)\dot{d}_{\mathrm{IF}}^{Ls0} - \hat{d}_{\mathrm{IF,GNSS}}^{Ls}}{c} \tag{10}$$

where $\widehat{dt}^{\,Ls}$ denotes the LEO satellite clock error solved in a post-processed precise clock determination procedure, and $\hat{d}_{\mathrm{IF,GNSS}}^{Ls}$ is the IF code hardware delay of the GNSS antenna onboard the LEO satellite, obtained based on the in-orbit calibration. d_{IF}^{Ls0} and $\dot{d}_{\mathrm{IF}}^{Ls0}$ denote the constant term (at a pre-defined reference temperature) and first-order derivative term (with respect to the temperature assuming it is available) of the LEO satellite downlink navigation signal antenna, respectively. T^{Ls} represents the temperature variation (with respect to the reference temperature) of the LEO satellite downlink navigation signal antenna. c is the speed of light.

2.1.2. Determination of the PCO and hardware delay increments for the downlink antenna. After the determination of the initial values for the hardware delays and orbits at the APCs for the downlink antenna, the increments of the PCOs and hardware delays compared to the on-ground calibration are estimated in the second step. With known coordinates of a Continuously Operating Reference Station, here the GNSS measurements are first used to determine the receiver clocks and the Zenith Wet Delays (ZWDs), e.g. via a PPP process [37, 38].

Using high-precision GNSS products and existing models for correction of the hydrostatic tropospheric delays, phase wind-ups, diverse tidal corrections, satellite and receiver antenna PCOs/PCVs, IF linear combination can be formed to

obtain high-accuracy station coordinates ($\hat{x}_r$), receiver clock error $\widehat{d\tilde{t}_r}$ at each epoch, and ZWD ($\hat{\tau}_r$) every few hours. Note that the estimated receiver clock error contains the IF receiver code bias for the GNSS signals used ($d_{\mathrm{IF,G}}$), which can be expressed as:

$$E\left(\widehat{d\tilde{t}_r}\right) = dt_r + \frac{d_{IF,G}}{c} \tag{11}$$

where E(·) is the expectation operator, and dt_r denotes the true receiver clock error.

The observation equations are then established for the estimation of the PCO (in IF combination) and the IF hardware delays of the downlink antenna. Parameters such as $\hat{x}_r$, $\widehat{d\tilde{t}_r}$, $\hat{\tau}_r$, $\hat{x}^{Ls0}$ and $\overset{\frown}{\breve{dt}}^{Ls0}$ are corrected in the O-C term ($\Delta p_{r,\mathrm{IF}}^{Ls}$ and $\Delta\varphi_{r,\mathrm{IF}}^{Ls}$). The downlink navigation signals of the LEO satellite are assumed to be dual-frequency signals, and the IF O-C terms in epoch t_i can be expressed as:

$$\begin{aligned} E\left(\Delta p_{r,\mathrm{IF}}^{Ls}(t_i)\right) &= \left(\mu_r^{Ls}(t_i)\right)^{\mathrm{T}} R_{\mathrm{NEU2ECEF}}(t_i)\ \delta x_{\mathrm{PCO}}^{Ls} \\ &\quad - \left(\delta\tilde{d}_{\mathrm{IF}}^{Ls} + T^{Ls}(t_i)\,\delta\dot{d}_{\mathrm{IF}}^{Ls}\right) \end{aligned} \tag{12}$$

$$\begin{aligned} E\left(\Delta\varphi_{r,\mathrm{IF}}^{Ls}(t_i)\right) &= \left(\mu_r^{Ls}(t_i)\right)^{\mathrm{T}} R_{\mathrm{NEU2ECEF}}(t_i)\ \delta x_{\mathrm{PCO}}^{Ls} \\ &\quad + \lambda_{\mathrm{IF}}\tilde{N}_{r,\mathrm{IF}}^{Ls} \end{aligned} \tag{13}$$

where $\delta x_{\mathrm{PCO}}^{Ls}$ denotes the increments of the in-orbit IF PCO compared to the on-ground calibration, and $\delta\dot{d}_{\mathrm{IF}}^{Ls}$ denotes the increment for the first-order IF code hardware delay with respect to the temperature for the downlink antenna. λ_{IF} denotes the IF wavelength of the LEO navigation signals. Since the GNSS PPP receiver clock bias $\widehat{d\tilde{t}_r}$ contains the IF code hardware delay of a certain GNSS (see equation (11)) when correcting the O-C term, $\delta\tilde{d}_{IF}^{Ls}$, needs to compensate for the corresponding GNSS IF code hardware delay, which can be described as:

$$\delta\tilde{d}_{\mathrm{IF}}^{Ls} = \delta d_{\mathrm{IF}}^{Ls} - d_{\mathrm{IF}} + d_{\mathrm{IF,G}}\ . \tag{14}$$

The unit direction vector from the LEO satellite to the ground station can be expressed as:

$$\mu_r^{Ls}(t_i) = \frac{\hat{x}_r - \hat{x}^{Ls0}(t_i)}{\left\|\hat{x}_r - \hat{x}^{Ls0}(t_i)\right\|}. \tag{15}$$

The estimable IF ambiguity $\tilde{N}$_(r,IF)^Ls can be formulated as:

$$\tilde{N}_{r,\mathrm{IF}}^{Ls} = N_{r,\mathrm{IF}}^{Ls} + \frac{\delta_{r,\mathrm{IF}} - \delta_{\mathrm{IF}}^{Ls} - d_{\mathrm{IF,G}}}{\lambda_{\mathrm{IF}}} \tag{16}$$

where $N_{r,IF}^{Ls}$ is the IF integer ambiguity, $\delta_{r,\mathrm{IF}}$ and $\delta_{\mathrm{IF}}^{Ls}$ denote the receiver and LEO satellite IF phase hardware delays, respectively. Based on the above observation equations, $\delta x_{\mathrm{PCO}}^{Ls}$, $\delta\tilde{d}_{IF}^{Ls}$ and $\delta\dot{d}_{\mathrm{IF}}^{Ls}$ can be obtained by solving a batch least-squares adjustment.

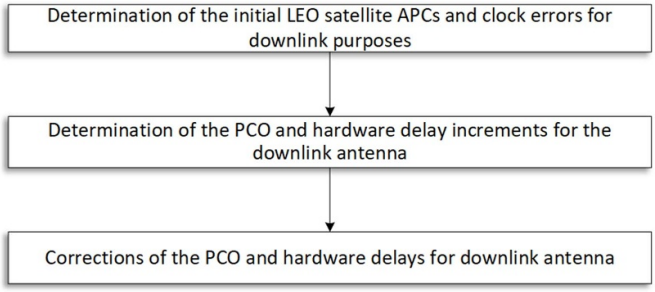

Figure 3. Flowchart of the in-orbit calibration of the PCO and hardware delays for the downlink antenna.

2.1.3. Corrections of the PCO and hardware delays for downlink antenna. The PCO ($\delta\hat{x}_{\mathrm{PCO}}^{Ls}$) and hardware delay ($\delta\tilde{d}_{IF}^{Ls}$ and $\delta\dot{d}_{\mathrm{IF}}^{Ls}$) of the LEO satellite downlink antenna can be calibrated in-orbit based on their initial values obtained in 2.1.1 and their increments estimated in 2.1.2:

$$\Delta\hat{x}_{\mathrm{PCO}}^{Ls} = \Delta\hat{x}_{\mathrm{PCO}}^{Ls0} + \delta\hat{x}_{\mathrm{PCO}}^{Ls} \tag{17}$$

$$\tilde{d}_{\mathrm{IF}}^{Ls} = d_{\mathrm{IF}}^{Ls0} + \delta\tilde{d}_{\mathrm{IF}}^{Ls} \tag{18}$$

$$\dot{d}_{\mathrm{IF}}^{Ls} = \dot{d}_{\mathrm{IF}}^{Ls0} + \delta\dot{d}_{\mathrm{IF}}^{Ls}. \tag{19}$$

It should be noted that $\tilde{d}_{IF}^{Ls}$ includes the difference between the receiver IF code hardware delay of the LEO satellite downlink navigation signals and GNSS signals, as described in equation (14).

As a summary, the process of in-orbit calibration of the PCO and hardware delays for the downlink antenna is illustrated by the flow chart depicted in figure 3.

2.2. Evaluation of formal precision and bias influence

The least-squares adjustment can be solved with the following equation:

$$\hat{X} = \left(A^T Q_{yy}^{-1} A\right)^{-1} A^T Q_{yy}^{-1} L \tag{20}$$

where the unknown vector $\hat{X}$ includes $\delta\hat{x}_{\mathrm{PCO}}^{Ls}$, $\delta\tilde{d}_{IF}^{Ls}$ and $\delta\dot{d}_{\mathrm{IF}}^{Ls}$, A is the design matrix containing the partial derivatives of the observations with respect to the unknowns, and it can be described by equations (21)–(25). Q_{yy} represents the observation variance-covariance matrix related to an elevation-dependent weight function, which can be expressed by equations (26), (27) and L denotes the O-C term, such that:

$$A = [A_1, \cdots, A_n]^T \tag{21}$$

$$A_i = \begin{bmatrix} \mu_i^T R_i & -e_m & -T & 0 \\ \mu_i^T R_i & 0 & 0 & \lambda_{\mathrm{IF}} I_m \end{bmatrix} \tag{22}$$

$$\mu_i = \left[\mu_i^{Ls}(t_1)^T, \cdots, \mu_i^{Ls}(t_m)^T\right]^T \tag{23}$$

$$R_i = \left[R_i^T(t_1), \cdots, R_i^T(t_m)\right]^T \tag{24}$$

$$T = \left[T(t_1), \cdots, T(t_m)\right]^T \tag{25}$$

where I_m is a unit matrix of size m, and e_m is a vector of ones with length m. λ_{IF} denotes the IF wavelength of the LEO navigation signals. $\mu_i^{Ls}(t_j)$ is the unit direction vector from the LEO satellite Ls to ground station i at epoch t_j. $T(t_j)$ represents the temperature variation with respect to the reference temperature of the LEO satellite downlink navigation signal antenna at epoch t_j, and $R_i(t_j)$ denotes the R_{NEU2ECEF} as described in equation (3). The variance-covariance matrix of the IF observations is expressed as:

$$Q_{yy}(i) = \frac{K \times (\sigma_0 \times \omega)^2}{\sin^2 E_i} \tag{26}$$

$$K = \frac{{f_1}^4 + {f_2}^4}{\left({f_1}^2 - {f_2}^2\right)^2} \tag{27}$$

where the zenith-referenced phase standard deviation (STD) σ_0 is set to 0.003 m, and K denotes the squared coefficient of IF combination, taken as 8.87 for L1 (1575.42 MHz) and L2 (1227.60 MHz) as examples here. f_1 and f_2 represent the two frequencies used. For code measurements, ω is set to 100 and for code observations, and equals 1 for phase measurements. E_i denotes the elevation angle from the ground station to the LEO satellite for the corresponding observation.

The formal precision of the estimated parameters (σ_{xx}) can be expressed as:

$$\sigma_{xx} = \sqrt{\left(A^T {Q_{yy}}^{-1} A\right)^{-1}}. \tag{28}$$

In addition to the formal precision, the mis-modeled bias (b) projected on the estimable parameters (b_u) is also evaluated:

$$b_u = \left(A^T {Q_{yy}}^{-1} A\right)^{-1} A^T {Q_{yy}}^{-1} b. \tag{29}$$

3. Test results

This section is divided into three parts. The first part deals with the simulation of the O-C terms for LEO satellite navigation signals. The satellite geometries of the LEO satellites Sentinel-6A (SEN6A) and Sentinel-3B (SEN3B), with inclinations of 66° and 98.65°, respectively, were used as examples to simulate the O-C terms of the downlink dual-frequency navigation signals on L1 (1575.42 MHz) and L2 (1227.60 MHz) as examples. Using the simulated signals, the second part of the section solves the PCOs and IF code hardware delays of the downlink signal antenna for different ground network distribution and processing periods, and evaluates their formal precision under different scenarios. The last part discusses the impact of typical mis-modeled biases on the estimable parameters. It is expected that the ground infrastructure tracking LEO satellite navigation signals would reach a certain density worldwide, like that for the GNSS. However, this would require changes in the current hardware, software, and even policies for signal usage in different countries, which might take some time. As such, it is conservatively assumed that the stations tracking LEO satellite navigation signals would be limited at the beginning phase, i.e. around 10 or fewer.

3.1. Simulation of the O-C terms

To solve the least-squares adjustment as described in section 2.2, the O-C terms of the phase and code observations are simulated for LEO satellites using the geometries from Sentinel-6A and Sentinel-3B on 1–6 February 2022 and 14–19 August 2018. As mentioned in section 2.1.2, receiver-related errors such as the receiver clock errors and the ZWDs are determined with the GNSS measurements. The difference between the IF receiver code hardware biases for the GNSS and the LEO satellite signals is considered in the LEO satellite IF hardware biases (see equation (14)). The Zenith Hydrostatic Delays, receiver PCOs/PCVs, phase windups, tidal effects are considered to be well modeled and corrected in the O-C terms. The first-order term of the ionosphere delays is eliminated by forming the IF combination. Hence, what is left to be considered in the simulated O-C terms are the phase and code observations noise, the phase ambiguities, the LEO satellite orbital and clock errors that bias the solutions, the LEO satellite downlink antenna's PCO, and temperature-related code hardware delays. The LEO satellite orbital and clock errors are simulated using the real Sentinal-6A satellite orbital and clock errors processed in near-real-time mode in a reduced-dynamic LEO satellite POD process [25], using the real-time GNSS products provided by the National Centre for Space Studies in France [39]. The orbits provided by the European Space Operations Centre were used as reference orbits [25], and the clocks post-processed using the final GNSS products from the Center for Orbit Determination in Europe with the reference orbits introduced, were used as reference clocks [40].

As shown in figure 4, the orbital errors can achieve a 1D Root Mean Square Error of a few centimeters, and clock errors can achieve a STD of 0.13 ns for Sentinel-6A on 5 February 2022 using the abovementioned processing settings. The corresponding daily RMS of the orbital errors and STD of the clock errors are illustrated in figure 5. It can be seen that in near-real-time, the three-dimensional (3D) RMS of orbital errors ranged mainly from 2.5 to 4 cm, while clock errors were generally between 3.2 and 6.2 cm (equivalent to 0.1–0.2 ns) over 6 d.

The PCO of the downlink navigation antenna is simulated as 0.01, 0.01 and 0.02 m in the antenna system (NEU) for the two LEO satellites based on reported cm-level differences between the on-ground and in-orbit calibration of Sentinel-6A [25]. The simulated hardware delays are illustrated in figure 6. It can be seen that the temperature variation of the LEO satellite antenna exhibits periodicity in orbit. Due to the short period of the orbit, approximately 100 min, and as it is unobstructed by the Earth during some periods, it is constantly

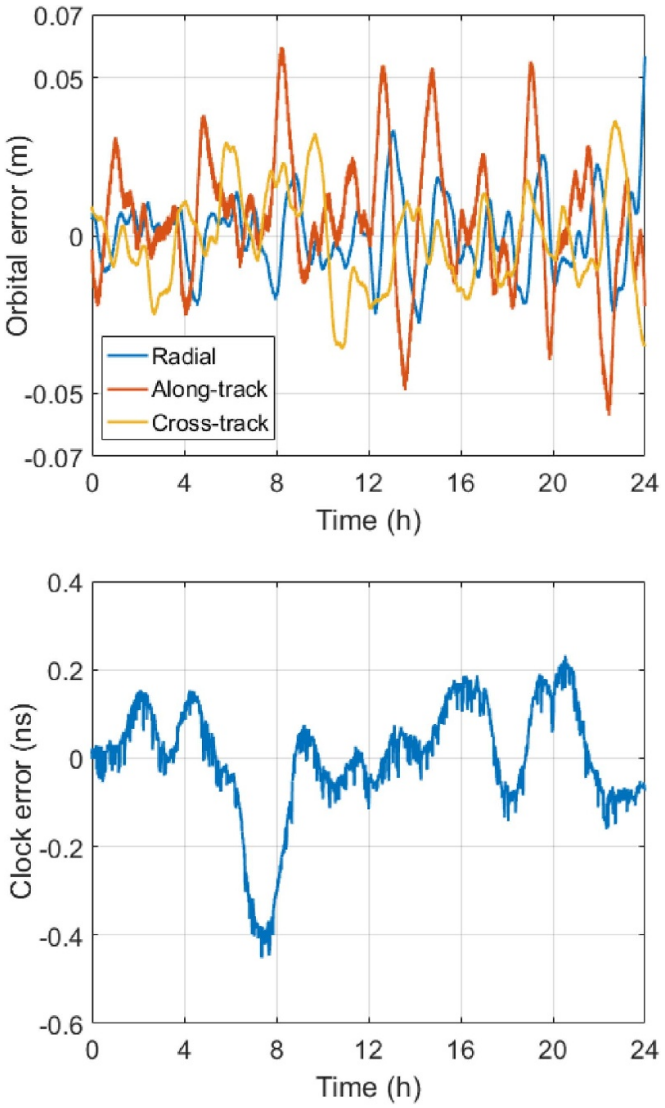

Figure 4. Orbital (top) and clock (bottom) errors of Sentinel-6A on 5 February 2022 in near-real-time.

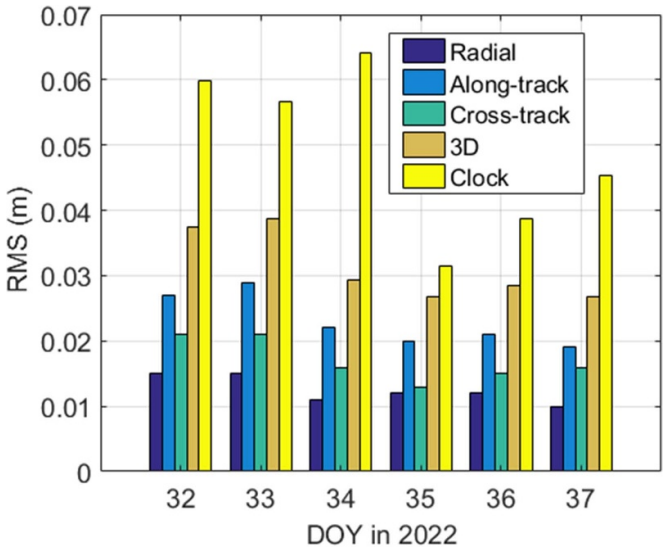

Figure 5. RMS of the orbital errors and STD of the clock errors for Sentinel-6A from 1 to 5 February 2022.

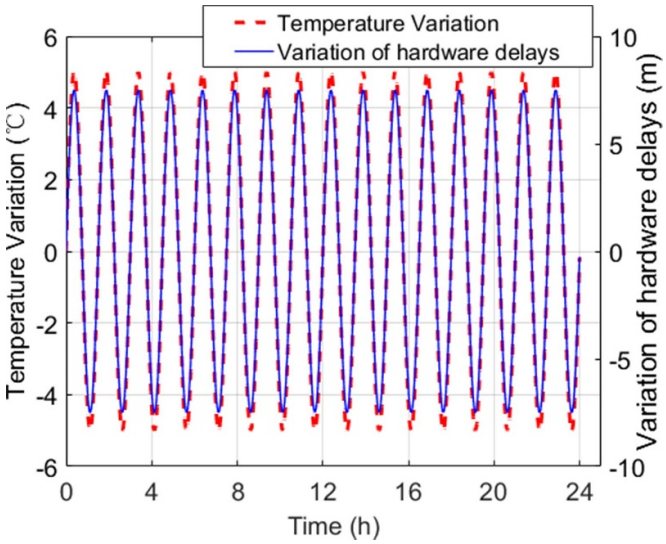

Figure 6. The simulated variation of the temperature and hardware delays for Sentinel-6A downlink antenna on 2 February 2022.

exposed to solar radiation, resulting in smooth temperature changes [41]. In this study, we use a simulated temperature variation period consistent with the orbital period, and assuming the amplitude of temperature variation is within ± 5 °C for both two test LEO satellites [41]. Figure 6 shows the simulated variation of the temperature and hardware delays for Sentinel-6A downlink antenna on 1 February 2022 as a representative example.

3.2. Analysis of the formal precision

This section is split into two parts, i.e. the analysis of the formal precision of the estimable parameters using the satellite geometry of Sentinel-6A with an inclination of 66°, and that of Sentinel-3B with near-polar orbits having an inclination of 98.65°. The sampling interval of the observations is 30 s. An elevation-mask angle of 5 degrees was set for tracking the LEO navigation signals.

3.2.1. Formal precision using the geometry of Sentinel-6A.

Figure 7 shows the ground tracks of the LEO satellite Sentinel-6A on 1 February 2022. A global ground network of 10 International GNSS Service stations [42], distributed in the areas between 66° N and 66° E, is assumed to be able to track the navigation signals from the LEO satellite. By analyzing the formal precision, the tracking stations used are increased sequentially, one by one, with the following sequence: XIA1, URUM, PTBB, YEL2, PERT, MGUE, MBAR, MKEA, STJ3, and OUS2.

Figure 8 shows formal precision of the North, East and Up components of the estimated downlink antenna's PCO using the geometry of the LEO satellite Sentinel-6A. It can be observed that both the number of tracking stations and the processing time impacted the formal precision. For a fixed

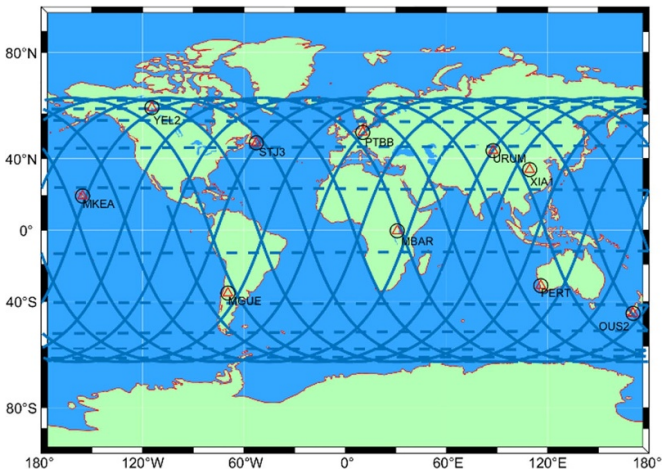

Figure 7. Ground network distribution and the ground tracks of the Sentinel-6A satellite.

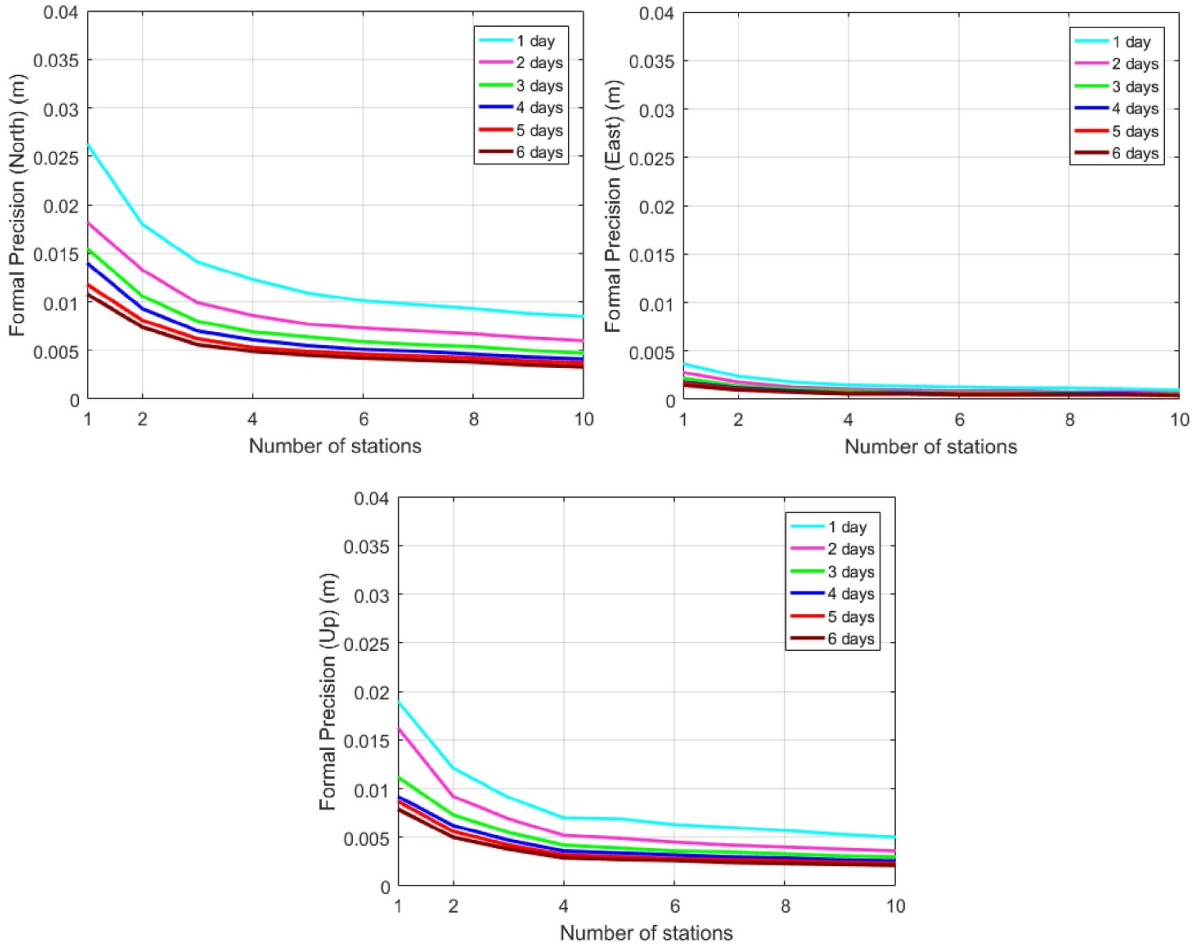

Figure 8. Formal precision of the North (top left), East (top right), and Up (bottom) components of the PCO of the downlink antenna. The geometry of the Sentinel-6A satellite was used for the calculation.

Table 1. The improvements of the three PCO components as the number of tracking stations increased from 1 to a certain number, for a processing time of 1 d.

PCO components	2 stations	4 stations	6 stations	8 stations	10 stations
North	32.2%	53.2%	61.8%	64.5%	67.9%
East	34.6%	59.2%	64.2%	67.9%	71.7%
Up	35.7%	62.5%	66.3%	69.7%	73.4%

Table 2. The improvements of the three PCO components as the processing time increased from 1 d to a certain number of days, with 5 tracking stations.

PCO Components	2 d	3 d	4 d	5 d	6 d
North	28.7%	41.0%	48.9%	55.0%	58.5%
East	28.5%	42.4%	50.2%	55.5%	59.5%
Up	28.8%	43.3%	51.0%	55.9%	60.1%

processing time, the formal precision becomes better as the number of tracking stations increases. This improvement is particularly obvious when the number of tracking stations is less than five. Taking the processing time of 1 d as an example for the North component (cyan line in the top left panel in figure 7), its formal precision is improved by 58% and 67.9%, respectively, when the number of tracking stations is increased from 1 to 5 and from 1 to 10. The improvements of the three PCO components (NEU) are summarized in table 1.

Similarly, for a fixed number of stations, the formal precision of all these components improves as the processing time increases. Taking the station number of five as an example, the formal precision of the North component improved by 28.7%, 41%, 48.9%, 55%, and 58.5%, respectively, when the processing time is increased from 1 d to 2, 3, 4, 5 and 6 d. The improvements of the three PCO components(NEU) are summarized in table 2.

From figure 8 it can be concluded that with a processing time of 3 d and 5 well-distributed tracking stations, the formal precision can reach about 7, 1, and 5 mm, respectively, for the North, East and Up PCO components. With a processing time of 6 d and 10 well-distributed tracking stations, the three components could achieve a formal precision of 3.3, 0.4 and 2.1 mm. The East component generally delivers better precision than the North and Up components. This is possibly caused by the assumption that the East direction of the downlink antenna is against the LEO satellite velocity direction (see section 2.1), which leads to a faster change in the corresponding partial derivatives of the design matrix. The decrease in the formal precision became less observed as the processing time increased to 4 d or more. It is worth noting that the distribution of the ground network plays an essential role in achieving good precision, and the empirical accuracy of the estimable parameters is often worse than the formal precision due to the disturbances of diverse mismodelled effects. The latter issue will be discussed in section 3.3.

Figure 9 shows the variation of the formal precision of the IF code hardware delay (D0) and its first-order derivative to the temperature (D1) with the station number and processing time. Similar to the PCO components, the number of tracking stations and processing time have significant impacts on the formal precision of D0 and D1. With a processing time of 3 d and 5 well-distributed tracking stations, the formal precision of D0 and D1 can reach 3.6 cm and 1.1 cm/°C, respectively. With a processing time of 6 d and 10 well-distributed tracking stations, the formal precision of D0 and D1 can reach 1.9 cm and 0.5 cm/°C, respectively. Unlike PCO, only code observations are involved in the calculation of D0 and D1. This leads to a worse formal precision of D0 and D1 than the PCO components under the same network distribution and processing periods.

3.2.2. Formal precision using the geometry of Sentinel-3B. In this sub-section, the formal precision of the estimable parameters is analyzed by taking the near-polar orbital geometry of the LEO satellite Sentinel-3B (with an inclination of 98.65°) as an example. Considering the larger latitude ranges of the ground tracks of Sentinel-3B compared to

Sentinel-6A (see figures 7 and 10), two more tracking stations in the North and South polar areas, respectively, THU2 and ARHT, were added to the 10 tracking stations used in section 3.2.1.

Figure 11 shows the impact of the number of tracking stations and the processing times on the formal precision of the North components of the PCO and the hardware delays D0 of the downlink antenna, as representative examples. For station numbers not higher than 10, the improvements of the PCO's formal precision are similar to those when using the Sentinel-6A satellite geometry. The formal precision of D0 and D1 have slightly degraded compared to that when using Sentinel-6A, i.e. amounting to about 2.9 cm and 0.9 cm/°C with 10 stations and 6 processing days. This is possibly caused by the decreased total visible time of the ground network to the Sentinel-3B than Sentinel-6A, i.e. from 2294 epochs to 1270 epochs.

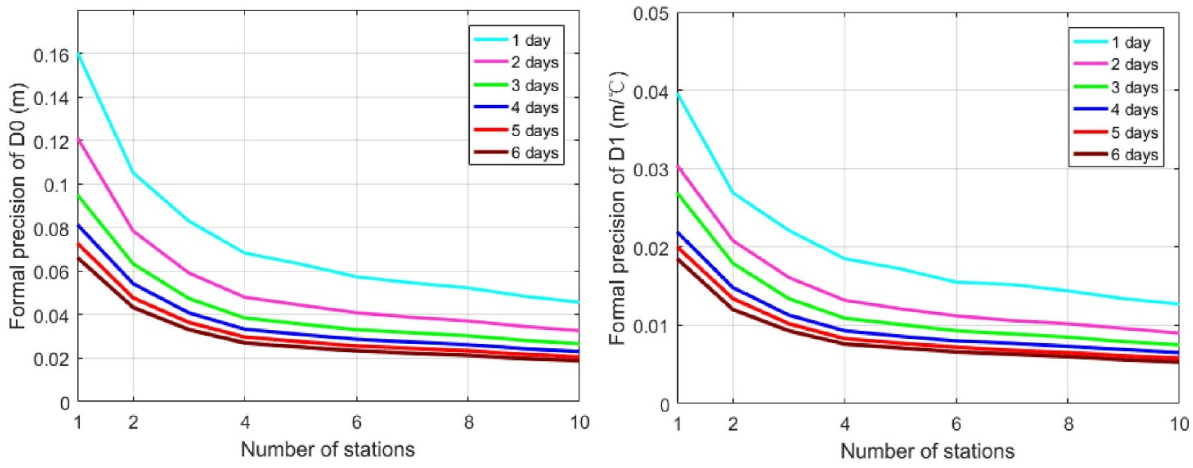

Figure 9. Formal precision of the hardware delays (D0 and D1) of the downlink navigation signal antenna. The geometry of the Sentinel-6A satellite was used for the calculation.

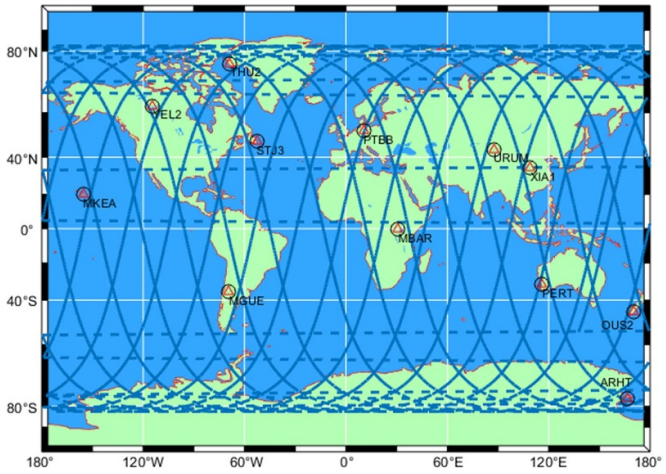

Figure 10. Ground network distribution and ground tracks of the Sentinel-3B satellite.

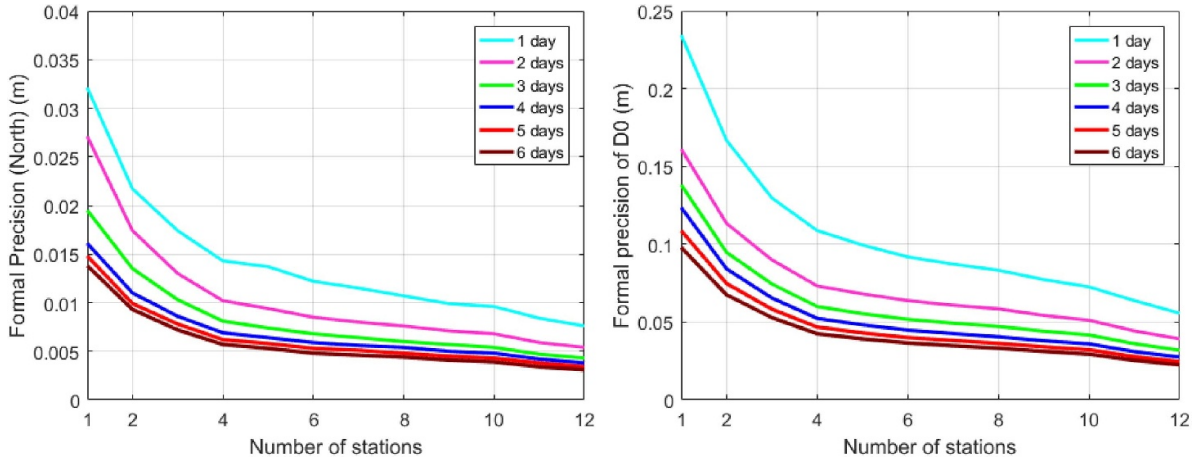

Figure 11. Formal precision of the North components of the PCO (left) and D0 (right) of the downlink antenna. The geometry of the Sentinel-3B satellite was used for the calculation.

After adding the two stations THU2 and ARHT in polar areas, relatively sharp improvements for all estimable parameters can be observed as shown in figure 11. With a processing time of 6 d and 12 well-distributed tracking stations, the three components achieve a formal precision of 3.1, 0.5 and 2.0 mm. The improvements in the formal precision of these parameters are summarized in figure 12 when adding more tracking stations, up to 12 stations, compared to the case of

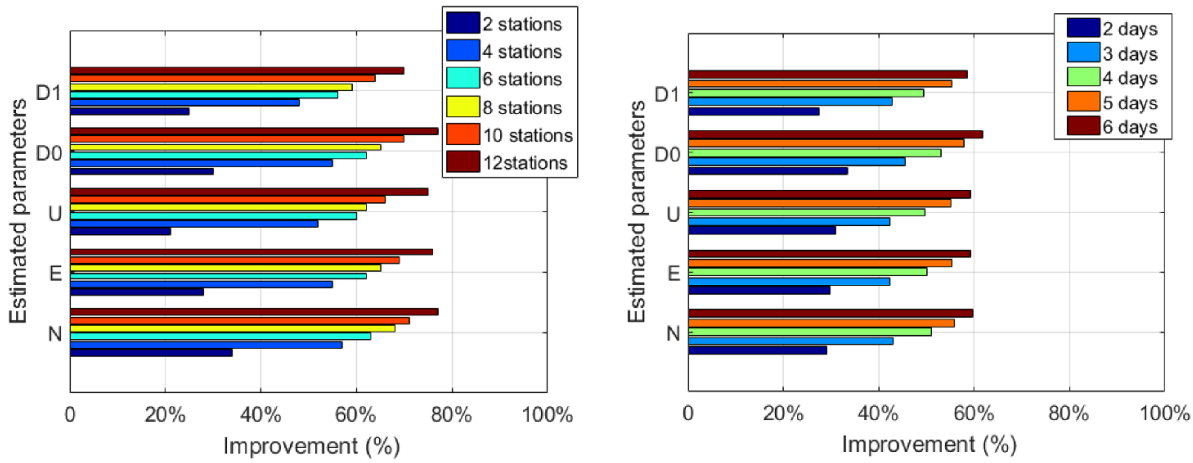

Figure 12. The improvements in formal precision for the North, East, Up components of the PCO and hardware D0 and D1 when increasing the tracking station number (left) or processing time (right).

Table 3. The improvements of the three PCO components, D0 and D1 as the number of tracking stations increased from 1 to a certain number, with a processing time of 1 d.

	Improvement (%)				
Number of stations	N	E	U	D0	D1
2	34.3%	28.3%	20.8%	30.4%	24.5%
4	57.3%	54.8%	52.2%	54.7%	48.0%
6	63.2%	61.7%	59.5%	61.7%	55.7%
8	67.6%	65.1%	62.3%	65.4%	58.7%
10	71.1%	68.9%	66.4%	69.7%	63.6%
12	76.8%	76.2%	75.3%	76.5%	70.1%

Table 4. The improvements of the three PCO components, D0 and D1 as the processing time increased from 1 d to a certain number of days, with 5 tracking stations.

	Improvement (%)				
Processing time (day)	N	E	U	D0	D1
2	29.1%	29.8%	30.9%	33.4%	27.5%
3	43.0%	42.3%	42.3%	45.6%	42.9%
4	51.0%	50.1%	49.6%	53.1%	49.4%
5	55.9%	55.4%	55.2%	58.0%	55.3%
6	59.7%	59.4%	59.4%	61.7%	58.6%

1 station (left panel), and when extending the processing time from 1 d to 6 d (right panel). The detailed improvements are given in tables 3 and 4. Taking the parameter D0 as an example, with a processing time of 1 d, the improvement of the formal precision amounts to about 61.7%, 65.4%, 69.7%, and 76.5%, when the station number is increased from 1 to 6, 8, 10 and 12, respectively. The stations in polar areas play an important role in the formal precision when the LEO satellite has near-polar orbits. This is caused by significantly increasing the visibility time when adding stations in polar areas, which add approximately 34.4% of the total observation epochs for the 12 stations.

3.3. Analysis of the effects of the biases

Compared to formal precision, mismodelled biases could lead to an unignorable, and even significant, impact on the empirical accuracy of the estimable parameters. For LEO navigation signals, diverse mismodelled effects could exist and bias the results, including multipath effects, the LEO satellite orbital and clock errors, and the variation of the receiver code hardware biases. In this section, the projection of LEO satellite orbital and clock errors in near-real-time is assessed.

The biases caused by LEO satellite orbital and clock errors are taken from a near-real-time reduced-dynamic LEO satellite

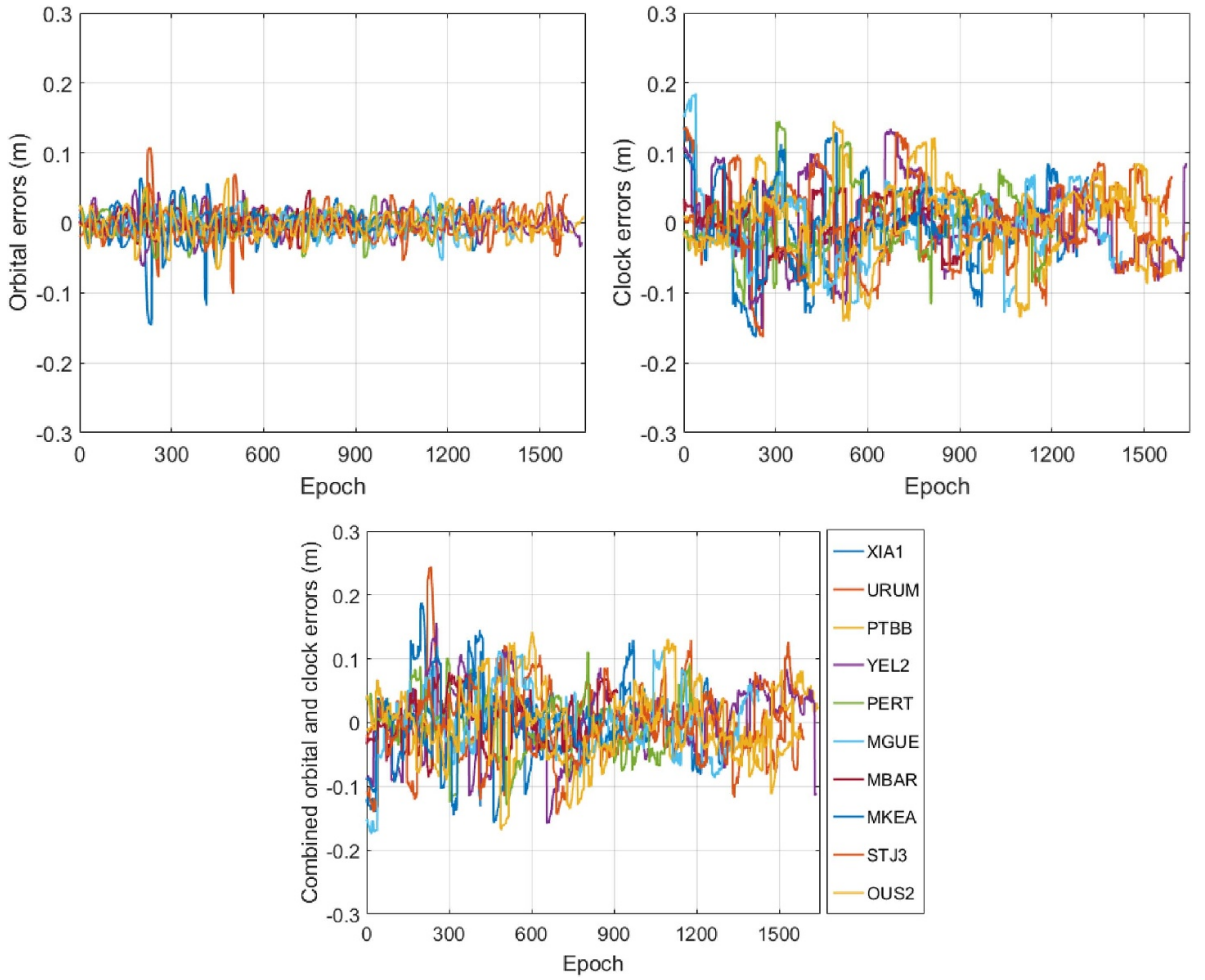

Figure 13. Projection of the LEO satellite orbital (top left), clock errors (top right) and their combined errors (bottom) in the signal direction.

POD process, as described in section 3.1. Figure 13 shows the projection of the LEO satellite orbital, clock errors, and their combined errors in the signal direction. The combined orbital and clock errors here refer to the LEO satellite clock errors subtracted from the 3D LEO satellite orbital errors projected into the signal direction. For users, the combined errors remain in the observation equations and represent a major error. A daily mean value was removed from the clock errors by calculation. It can be observed that the orbital and clock errors mainly range from a few centimeters to 1 dm. Table 5 lists the RMS of the projected orbital and clock errors for each station. Their results were close in general. The RMS of the satellite clock errors range from 3.8 to 5.3 cm (0.13–0.18 ns) and the projected orbital errors from 1.5 to 2 cm. The RMS of the combined satellite clock and orbital errors range from 4.0 to 5.6 cm.

Figure 14 depicts the impact of the combined LEO satellite orbital and clock errors on the PCOs and hardware delays (D0 and D1) when using different numbers of tracking stations and processing times based on the geometry of the Sentinel-6A satellite. It can be observed that increasing the number of stations generally strengthens the model and reduces the resulting biases in the estimated parameters. When the number of tracking stations increases to 10, the projected biases of all the PCO components are within 5 mm. When the processing time increases further, from 1 to 6 d, the biases are reduced to below 2 mm. For D0 and D1, it can also be observed that using 10 stations and 6 d for processing, the biases can be reduced to an insignificant level, i.e. below 2 mm. More detailed bias values are presented in tables 6 and 7, where a processing time of 1 d is used in table 6 and one tracking station is employed in table 7. With a processing time of 6 d and using 10 well-distributed tracking stations, the bias disturbances of the three PCO components and hardware delay D0 can be decreased to below 5 mm for Sentinal-3B. By adding two tracking stations in polar regions, the bias disturbances can be further decreased to below 3 mm. For the reason of comparison, the results for Sentinel-3B are also given in tables 6

Table 5. STD of the projected clock errors, RMS of the orbital errors and their combined errors in signal direction for each ground station.

Station	STD of the clock errors (m)	RMS of the projected orbital errors (m)	RMS of the combined errors (m)
XIA1	0.053	0.025	0.054
URUM	0.049	0.021	0.053
PTBB	0.048	0.015	0.047
YEL2	0.054	0.017	0.056
PERT	0.048	0.018	0.047
MGUE	0.053	0.016	0.054
MBAR	0.038	0.015	0.040
MKEA	0.053	0.018	0.056
STJ3	0.048	0.017	0.049
OUS2	0.049	0.019	0.052

and 7 using the same orbital and clock errors as described before. The general trend of the variation in the bias projection with the station number and processing time remains the same.

4. Discussions and conclusions

Benefiting from the significantly reduced altitudes of LEO satellites and their consequent higher speeds, LEO augmentation has become a prominent tool in enhancing traditional GNSS-based Positioning, Navigation, and Timing (PNT) services. However, to achieve high-accuracy PPP and timing on the ground using LEO navigation signals, it is imperative to accurately calibrate, model, or eliminate a variety of errors and biases present in the downlink navigation signals between LEO satellites and ground users. Similar to GNSS satellites, calibrating the PCOs and hardware delays of the LEO downlink signal transmitter/antenna in orbit necessitates the utilization of downlink navigation signals received by ground stations. Nevertheless, given the limited coverage areas of LEO satellites and the anticipated insufficiency of ground stations equipped to receive LEO navigation signals in the future, significant challenges are posed for the in-orbit calibration of these parameters.

In this study, an approach is proposed to calculate the PCO and hardware delay of the downlink navigation antenna for LEO satellites making use of the GNSS and LEO dual-frequency navigation signals. The formal precision and bias disturbances are analyzed for the estimable parameters using different LEO satellite geometries, under different ground network distributions and processing times.

For example, for the Sentinel-6A satellite with an inclination of about 66 degrees and the Sentinel-3B satellite with a near-polar orbit, increasing the number of tracking stations and processing time can both improve the formal precision of the PCO components and the hardware delay parameters (D0 and D1). Taking the North PCO component as an example, as the processing time increased by one-day increments, from 1 to 6 d, the improvements when using 5 well-distributed tracking stations amount to 32.2%, 53.2%, 61.8%, 64.5%, 67.9% for Sentinel-6A and 29.1%, 43.0%, 51.0%, 55.9%, 59.7% for Sentinel-3B, respectively. As the number of tracking stations increased from 1 to 2, 4, 6, 8 and 10, the improvements in processing one day of data amount to 32.2%, 53.2%, 61.8%, 64.5% and 67.9% for Sentinel-6A and 34.3%, 57.3%, 63.2%, 67.6%, 76.8% for Sentinel-3B, respectively. With a processing time of 6 d and 10 well-distributed tracking stations, the three PCO components could achieve a formal precision of 3.3, 0.4 and 2.1 mm for Sentinel-6A and 3.9, 0.6, 2.7 mm for Sentinel-3B. The hardware delay D0 and D1 could achieve a formal precision of 1.9 cm, 5.3 mm/°C for Sentinel-6A, and 2.9 cm and 8.3 mm/°C for Sentinel-3B, respectively. After adding two stations in polar areas for Sentinel-3B, relatively sharp improvements can be observed in all estimable parameters. With a processing time of 6 d and 12 well-distributed tracking stations, the three PCO components could achieve a formal precision of 3.1, 0.5, and 2.0 mm. Hence, for LEO satellites of near-polar orbits, ground tracking stations at polar areas are important for the observation model and formal precision.

Using the real LEO satellite orbital and clock errors processed in a near-real-time mode, the impacts of the biases induced by LEO satellite POD and clock determination were also assessed for the PCOs and hardware delays (D0 and D1). As the number of tracking stations and the processing time increases, the bias disturbances in the three PCO components and hardware delays (D0, D1) decrease. With a processing time of 6 d and using 10 well-distributed tracking stations, the bias disturbances on the three PCO components and hardware delay D0 can be decreased to below 2 mm for Sentinel-6A, and 3 mm for Sentinel-3B, respectively. Finally, when adding two tracking stations in polar regions for Sentinel-3B, the bias disturbances of the three PCO components and hardware delay D0 can also be decreased to below 2 mm.

There are remaining issues that could lead to differences between the formal precision of the parameters analyzed in this study and their empirical accuracies using real LEO satellite navigation signals in the future. For example, a temperature-related linear polynomial might not completely

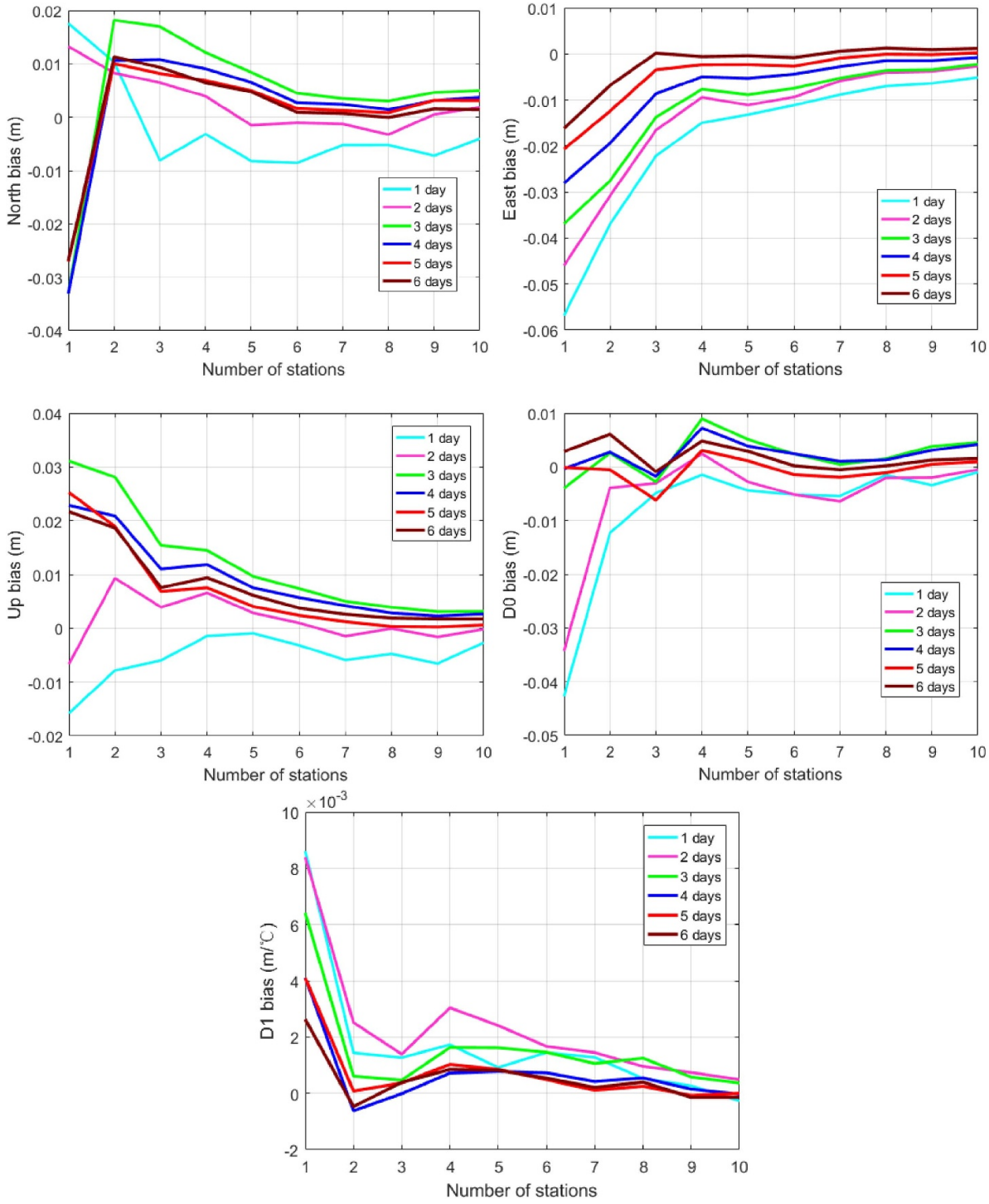

Figure 14. The biases induced by the Sentinal-6A satellite orbital and clock errors on the North (top left), East (top right), and Up (middle left) components of the PCOs, and the D0 (middle right) and D1 (bottom) terms of the code hardware delays.

Table 6. Biases in the three PCO components, D0 and D1 when increasing the number of the tracking stations from 2 to 10, with a processing time of one day.

	Sentinel-6A					Sentinel-3B				
Number of stations	North PCO (m)	East PCO (m)	Up PCO (m)	D0 (m)	D1 (m/°C)	North PCO (m)	East PCO (m)	Up PCO (m)	D0 (m)	D1 (m/°C)
2	0.010	−0.037	−0.008	−0.012	0.001	0.020	0.001	0.017	0.003	0.001
4	−0.003	−0.015	−0.001	−0.001	0.002	0.015	0.004	0.007	0.007	0.000
6	−0.009	−0.011	−0.003	−0.005	0.001	0.009	−0.001	0.008	0.000	−0.002
8	−0.005	−0.007	−0.005	−0.002	0.001	−0.007	0.003	0.007	0.001	−0.001
10	−0.004	−0.005	−0.003	−0.001	−0.000	−0.003	0.002	0.004	0.000	−0.001

Table 7. Biases in the three PCO components, D0 and D1 when increasing the processing time from 1 to 6 d using one tracking station.

	Sentinel-6A					Sentinel-3B				
Processing time (day)	North PCO (m)	East PCO (m)	Up PCO(m)	D0 (m)	D1 (m/°C)	North PCO (m)	East PCO (m)	Up PCO (m)	D0 (m)	D1 (m/°C)
1	0.018	−0.057	−0.016	−0.043	0.009	0.078	0.001	0.032	0.023	0.002
2	0.013	−0.046	−0.007	−0.034	0.008	0.044	0.001	0.015	0.027	0.003
3	−0.033	−0.037	0.031	−0.004	0.006	0.029	0.004	0.013	0.032	−0.002
4	−0.033	−0.028	−0.023	0.000	0.004	0.026	0.004	0.010	0.025	−0.002
5	−0.027	−0.021	0.025	0.000	0.004	0.025	0.000	0.007	0.019	−0.002
6	−0.027	−0.016	0.022	0.003	0.003	0.026	−0.002	0.008	0.020	0.000

cover the variations of the hardware delays. Its variation model with the temperature could be more complicated, and the hardware delays could be further influenced by other factors like changes in voltage. Futurer studies will investigate these issues when real LEO satellite navigation data become available.

Data availability statement

The data of SENTINEL-3B and SENTINEL-6A were obtained from the Copernicus Data Space Ecosystem. The real -time GNSS products were obtained from the National Centre for Space Studies in France (CNES). The GNSS final products were obtained from the Center for Orbit Determination in Europe (CODE).

Acknowledgments

This work is supported by the International Partnership Program of the Chinese Academy of Sciences. Grant No. 021GJHZ2023010FN. The work is also funded by the National Time Service Center, Chinese Academy of Sciences (CAS) (No. E167SC14), the National Natural Science Foundation of China (No. 12073034), and the Australian Research Council—Discovery Project No. DP240101710. We would like to acknowledge the support of the international GNSS monitoring and assessment system (iGMAS) at the National Time Service Center, and the National Space Science Data Center, National Science & Technology Infrastructure of China (www.nssdc.ac.cn).

ORCID iDs

Jiawei Liu https://orcid.org/0009-0008-3062-8356
Kan Wang https://orcid.org/0000-0001-5688-6937
Ahmed El-Mowafy https://orcid.org/0000-0001-7060-4123

References

[1] Reid T G R, Neish A M, Walter T and Enge P K 2018 Broadband LEO constellations for navigation *Navigation J. Jpn. Inst. Navig.* **65** 205–20
[2] Su Y, Liu Y, Zhou Y, Yuan J, Cao H and Shi J 2019 Broadband LEO satellite communications: architectures and key technologies *IEEE Wirel. Commun.* **26** 55–61
[3] Sandau R 2010 Status and trends of small satellite missions for earth observation *Acta Astronaut.* **66** 1–12
[4] Michalak G, Glaser S, Neumayer K H and König R 2021 Precise orbit and earth parameter determination supported by LEO satellites, inter-satellite links, and synchronized clocks of a future GNSS *Adv. Space Res.* **12** 4753–82
[5] Li W, Yang Q, Du X, Li M, Zhao Q, Yang L, Qin Y, Chang C, Wang Y and Qin G 2023 LEO augmented precise point positioning using real observations from two CENTISPACE™ experimental satellites *GPS Solut.* **28** 44
[6] Zhang X and Ma F 2019 Overview of development on low earth orbit navigation augmentation GNSS *Acta Geod. Cartograph. Sin.* **48** 1073–87
[7] Lawrence D, Cobb H S, Gutt G, O'Connor M, Reid T G R, Walter T and Whelan D 2017 Innovation: navigation from LEO (GPS World) (available at: www.gpsworld.com/innovation-navigation-from-leo/) (Accessed 10 October 2022)
[8] Li X, Ma F, Li X, Lv H, Bian L, Jiang Z and Zhang X 2018 LEO constellation-augmented multi-GNSS for rapid PPP convergence *J. Geod.* **93** 749–64

[9] Li M, Xu T, Guan M, Gao F and Jiang N 2022 LEO-constellation-augmented multi-GNSS real-time PPP for rapid re-convergence in harsh environments *GPS Solut.* **26** 29

[10] Wang K, El-Mowafy A, Wang W, Yang L and Yang X 2022 Integrity monitoring of PPP-RTK positioning; part II: LEO augmentation *Remote Sens.* **14** 1599

[11] Faragher R and Ziebart M 2020 OneWeb LEO PNT: progress or risky gamble? Inside GNSS (available at: https://insidegnss.com/oneweb-leo-pnt-progress-or-risky-gamble/) (Accessed 28 June 2021)

[12] Jia Y, Bian L, Cao Y, Meng Y and Zhang L 2020 Design and Analysis of Beidou Global Integrity System Based on LEO Augmentation *China Satellite Navigation Conf. (CSNC) 2020 Proc., Volume II. CSNC 2020* (*Lecture Notes in Electrical Engineering*) vol 651, ed J Sun, C Yang and J Xie (Springer) pp 624–33

[13] Geng J, Guo J, Wang C and Zhang Q 2021 Satellite antenna phase center errors: magnified threat to multi-frequency PPP ambiguity resolution *J. Geod.* **95** 72

[14] Gu S, Dang Y, Wang H, Wang J, Ren Z and Zhang J 2019 The effect of DCB correction on multi-system combination precise point positioning *China Satellite Navigation Conf. (CSNC) 2019 Proc CSNC 2019* (*Lecture Notes in Electrical Engineering* vol 562) ed J Sun, C Yang and Y Yang (Springer)

[15] Guillermo T *et al* 2014 magicGNSS' real-time POD and PPP multi-GNSS service *Proc. 27th Int. Technical Meeting of the Satellite Division of the Institute of Navigation (ION GNSS+ 2014)* (*Tampa, Florida*, *September 2014*) pp 1046–55

[16] Lou Y, Dai X, Gong X, Li C, Qing Y, Liu Y, Peng Y and Gu S 2022 A review of real-time multi-GNSS precise orbit determination based on the filter method *Satell. Navig.* **3** 15

[17] Li M, Wei K, Xu T, Shi Y and Wang D 2023 Enhanced precise orbit determination for GPS and BDS-2/3 with real LEO onboard and ground observations *Measurement* **224** 113912

[18] Zeng T, Sui L, Ruan R, Jia X, Feng L and Xiao G 2021 GPS triple-frequency undifferenced and uncombined precise orbit determination with the consideration of receiver time-variant bias *Measurement* **169** 108281

[19] Zhang Y, Li Z, Wang Z, Li R and Yuan H 2021 The improvement of BDS observation geometry with LEO constellations in orbit determination *Measurement* **177** 109228

[20] Choi B K, Cho J H and Lee S J 2011 Estimation and analysis of GPS receiver differential code biases using KGN in Korean Peninsula *Adv. Space Res.* **47** 1590–9

[21] Montenbruck O, Hauschild A and Steigenberger P 2014 Differential code bias estimation using multi-GNSS observations and global ionosphere maps *J. Inst. Navig.* **61** 191–201

[22] Liu T, Zhang B, Yuan Y, Li Z and Wang N 2019 Multi-GNSS triple-frequency differential code bias (DCB) determination with precise point positioning (PPP) *J. Geod.* **93** 765–84

[23] Wang K, Liu J, Su H, El-Mowafy A and Yang X 2023 Real-time LEO satellite orbits based on batch least-squares orbit determination with short-term orbit prediction *Remote Sens.* **15** 133

[24] Wang K and El-Mowafy A 2022 LEO satellite clock analysis and prediction for positioning applications *Geo-Spatial Inf. Sci.* **25** 14–33

[25] Montenbruck O, Hackel S, Wermuth M and Zangerl F 2021 Sentinel-6A precise orbit determination using a combined GPS/Galileo receiver *J. Geod.* **95** 109

[26] Coster A, Williams J, Weatherwax A, Rideout W and Herne D 2013 Accuracy of GPS total electron content: GPS receiver bias temperature dependence *Radio Sci.* **48** 190–6

[27] Zhang B and Teunissen P J 2015 Characterization of multi-GNSS between-receiver differential code biases using zero and short baselines *Sci. Bull.* **60** 1840–9

[28] Mao X, Arnold D, Girardin V, Villiger A and Jäggi A 2021 Dynamic GPS-based LEO orbit determination with 1 cm precision using the bernese GNSS software *Adv. Space Res.* **67** 788–805

[29] Allahvirdi-Zadeh A, Wang K and El-Mowafy A 2021 POD of small LEO satellites based on precise real-time MADOCA and SBAS-aided PPP corrections *GPS Solut.* **25** 31

[30] Montenbruck O, Hauschild A, Andres Y, von Engeln A and Marquardt C 2013 (Near-) real-time orbit determination for GNSS radio occultation processing *GPS Solut.* **17** 199–209

[31] Hauschild A, Tegedor J, Montenbruck O, Visser H and Markgraf M 2016 Precise onboard orbit determination for LEO satellites with real-time orbit and clock corrections *Proc. ION GNSS+ 2016* (*Portland, Oregon, USA*, *12–16 September*) (Institute of Navigation) pp 3715–23

[32] Gong X, Zhang W, Wang Q, Wang F, Li X, Sang J and Liu W 2022 Precise real-time navigation of the small TJU-1 satellite using GPS, GLONASS and BDS *Measurement* **204** 112090

[33] Wang Z, Li Z, Wang L, Wang N, Yang Y, Li R, Zhang Y, Liu A, Yuan H and Hoque M 2022 Comparison of the real-time precise orbit determination for LEO between kinematic and reduced-dynamic modes *Measurement* **187** 110224

[34] Li X, Zhang K, Meng X, Zhang W, Zhang Q, Zhang X and Li X 2020 Precise orbit determination for the FY-3C satellite using onboard BDS and GPS observations from 2013, 2015, and 2017 *Engineering* **6** 904–12

[35] Shoemake K 1985 Animating rotation with quaternion curves *Proc. 12th Annual Conf. on Computer Graphics and Interactive Techniques* pp 245–54

[36] Wang K, Su H, El-Mowafy A and Yang X 2023 Prediction and ephemeris fitting of LEO navigation satellites orbits computed at the antenna phase center *Measurement* **224** 113935

[37] Zumberge J F, Heflin M B, Jefferson D C, Watkins M M and Webb F H 1997 Precise point positioning for the efficient and robust analysis of GPS data from large networks *J. Geophys. Res.* **102** 5005–17

[38] Kouba J and Héroux P 2001 Precise point positioning using IGS orbit and clock products *GPS Solut.* **5** 12–28

[39] Dach R, Schaer S, Arnold D, Kalarus M S, Prange L, Stebler P, Villiger A and Jäggi A 2020 CODE rapid product series for the IGS (Published by Astronomical Institute, University of Bern) (https://doi.org/10.7892/boris.75854.4)

[40] Švehla D and Rothacher M 2003 Kinematic and reduced-dynamic precise orbit determination of low earth orbiters *Adv. Geosci.* **1** 47–56

[41] Shangkun Z, Anqi H and Jie L 2017 Analysis of in-orbit thermal-induced vibration of earth low-orbit satellite antenna *Noise Vib. Control* **37** 213–6

[42] Johnston G, Riddell A and Hausler G 2017 The international GNSS service *Springer Handbook of Global Navigation Satellite Systems* 1st edn, ed J G Teunissen Peter and O Montenbruck (Springer) pp 967–82